Cyclic Electron Transfer within the [Zn-Myoglobin, Cytochrome b_5] Complex

Judith M. Nocek,[†] Bhavini P. Sishta,[†] Janelle C. Cameron,[†] A. Grant Mauk,[‡] and Brian M. Hoffman[†,*]

Contribution from the Department of Chemistry, Northwestern University, Evanston, Illinois 60208-3113, and Department of Biochemistry and Molecular Biology, University of British Columbia, Vancouver, British Columbia, V6T 1Z3, Canada

Received September 3, 1996[⊗]

Abstract: To characterize the electrostatic complex formed between myoglobin (Mb) and cytochrome b_5 (Feb_5), we have performed flash photolysis triplet-quenching and electron-transfer (ET) measurements of the interaction between Zn deuteroporphyrin (ZnD)-substituted Mb (sperm whale) (ZnDMb) and Feb_5(trypsin-solubilized, bovine) at pH values between 6 and 7.5. For pH values between pH 6 and pH 7.5, the quenching rate constant (Δk) varies linearly with [$Fe^{3+}b_5$]. The slope (M) obtained from plots of Δk versus [$Fe^{3+}b_5$] is strongly dependent on pH ($M = 140 \times 10^6$ M^{-1} s^{-1} at pH 6 and $M = 2.4 \times 10^6$ M^{-1} s^{-1} at pH 7.5). The triplet decay profiles remain exponential throughout these titrations. Together, these results indicate that the association constant obeys the inequality, $K_a \leq 3000$ M^{-1} and that the lower limit for the rate constant for dissociation of the ^{3}**DA** complex of $(k_{off})_{min} = 10^6$ s^{-1} at pH 6 and $(k_{off})_{min} = 10^4$ s^{-1} at pH 7.5. Transient absorption measurements have shown that this quenching of ^{3}ZnDMb by $Fe^{3+}b_5$ can be attributed to intracomplex ^{3}ZnD → Fe^{3+}P ET and that the transient absorbance changes observed at the ^{3}**D**/**D** isosbestic points represent the time evolution of the ($\boldsymbol{D}^+\boldsymbol{A}^-$), [ZnD$^+$Mb, $Fe^{2+}b_5$] intermediate, **I**. The long-time behavior of the progress curves ($t \geq 20$ ms) collected during a titration of $Fe^{3+}b_5$ by ZnDMb (reverse titration protocol) is neither purely second-order nor purely first-order but rather resembles a mixed-order process involving both the ($\boldsymbol{D}^+\boldsymbol{A}^-$) complex and its dissociated components. Modeling this data indicates that the $\boldsymbol{D}^+\boldsymbol{A}^-$ complex product must dissociate with a rate constant slower than that of the precursor, **DA**, complex. Theoretical studies of the protein pair by Brownian dynamics simulations show that Mb has a broad reactive surface which encompasses the "hemisphere" that includes the exposed heme edge. The most stable complexes occur when b_5 is bound at one of two subdomains within this hemisphere. The kinetics measurements and calculations taken together allow us to discuss the relative importance of global and local electrostatics in regulating protein−protein recognition and reactivity.

Introduction

Ferrous myoglobin (Fe^{2+}Mb), a heme-protein found in skeletal and heart muscle tissues, functions in the transport of oxygen to the mitochondria and in short-term oxygen storage.[1−3] Under physiological conditions, both oxyMb and deoxyMb can be oxidized to the inactive metMb (Fe^{3+}Mb).[4] It has been suggested that Fe^{3+}Mb is maintained at low levels by a reductase system in which cytochrome b_5 (b_5) is the final electron donor to Fe^{3+}Mb.[5,6]

$$Fe^{3+}Mb + Fe^{2+}b_5 \rightarrow Fe^{2+}Mb + Fe^{3+}b_5 \qquad (1)$$

This reaction appears to involve the formation of a specific protein−protein complex[7,8] between Fe^{3+}Mb and $Fe^{2+}b_5$, but the mechanism of electron transfer (ET) between these physiological partners has not been investigated in detail. Protein−protein complexes often adopt multiple conformational states in solution.[9−17] Therefore, a full kinetic mechanism for electron transfer must incorporate details of the dynamics of conformational interconversion within the complex as well as of the actual intracomplex ET event.

[†] Northwestern University.
[‡] University of British Columbia.
[⊗] Abstract published in *Advance ACS Abstracts*, February 1, 1997.

(1) Livingstone, D. J.; LaMar, G. N.; Brown, W. D. *Science* **1983**, *220*, 71−73.
(2) Wittenberg, J. B. *Physiol. Rev.* **1970**, *50*, 559−636.
(3) *Hemoglobin and Myoglobin in Their Reactions with Ligands*, Antonini, E., Brunori, M., Eds.; North Holland Publishing Co.: Amsterdam, 1971.
(4) Brantley, R. E., Jr.; Smerdon, S. J.; Wilkinson, A. J.; Singleton, E. W.; Olson, J. S. *J. Biol. Chem.* **1993**, *268*, 6995−7010.
(5) Hickson, R. C.; Rosenkoetter, M. A. *Am. J. Physiol.* **1981**, *241*, C140−C144.
(6) Hagler, L.; Coppes, R. I., Jr.; Herman, R. H. *J. Biol. Chem.* **1979**, *254*, 6505−6514.
(7) Stayton, P. S.; Fisher, M. T.; Sligar, S. G. *J. Biol. Chem.* **1988**, *263*, 13544−13548.
(8) Livingston, D. J.; McLachlan, S. J.; La Mar, G. N.; Brown, W. D. *J. Biol. Chem.* **1985**, *260*, 15699−15707.
(9) Hoffman, B. M.; Ratner, M. A.; Wallin, S. A. In *Advances in Chemistry Series*; Johnson, M. K., King, R. B., Kurtz, D. M., Jr., Kutal, C., Norton, M. L., Scott, R. A., Eds.; American Chemical Society: Washington, D.C., 1990; pp 125−146.
(10) Zhou, J. S.; Kostíc, N. M. *J. Am. Chem. Soc.* **1993**, *115*, 10796−10804.
(11) Nocek, J. M.; Stemp, E. D. A.; Finnegan, M. G.; Koshy, T. I.; Johnson, M. K.; Margoliash, E.; Mauk, A. G.; Smith, M.; Hoffman, B. M. *J. Am. Chem. Soc.* **1991**, *113*, 6822−6831.
(12) Moser, C. C.; Dutton, P. L. *Biochemistry* **1988**, *27*, 2450−2461.
(13) Willie, A.; Stayton, P. S.; Sligar, S. G.; Durham, B.; Millett, F. *Biochemistry* **1992**, *31*, 7237−7242.
(14) McLendon, G.; Pardue, K.; Bak, P. *J. Am. Chem. Soc.* **1987**, *109*, 7540−7541.
(15) Mauk, M. R.; Mauk, A. G.; Weber, P. C.; Matthew, J. B. *Biochemistry* **1986**, *25*, 7085−7091.
(16) Mauk, A. G. *Struct. Bonding* **1991**, *75*, 131−157.
(17) Everest, A. M.; Wallin, S. A.; Stemp, E. D. A.; Nocek, J. M.; Mauk, A. G.; Hoffman, B. M. *J. Am. Chem. Soc.* **1991**, *113*, 4337−4338.

S0002-7863(96)03081-8 CCC: $14.00

To characterize the electrostatic complex formed between Mb and b_5, we have used flash photolysis to study both triplet-quenching and electron-transfer between ZnDMb(sperm whale) and Feb_5(trypsin-solubilized, bovine) at pH values between 6 and 7.5. The Zn porphyrin in ZnDMb, which is a structural analogue of the heme in Fe^{2+}Mb, has a long-lived triplet excited state (^{3}ZnD) that is a strong reducing agent.[18,19] Intracomplex ^{3}ZnD(**^{3}D**) → Fe^{3+}P(**A**) ET quenching (eq 2) is studied

$$\underset{\mathbf{^3DA}}{[^3\text{ZnDMb, Fe}^{3+}b_5]} \rightarrow \underset{\mathbf{I}}{[\text{ZnD}^{+}\text{Mb, Fe}^{2+}b_5]} \qquad (2)$$

by monitoring the ^{3}ZnDMb/ZnDMb transient absorbance difference. The [ZnD^+Mb, $Fe^{2+}b_5$] charge-transfer intermediate (**I**) returns to the initial state by intracomplex electron transfer from $Fe^{2+}b_5$ to ZnD^+Mb (eq 3),

$$\underset{\mathbf{I}}{[\text{ZnD}^{+}\text{Mb, Fe}^{2+}b_5]} \rightarrow \underset{\mathbf{DA}}{[\text{ZnDMb, Fe}^{3+}b_5]} \qquad (3)$$

and is studied by monitoring the transient absorbance changes at the ^{3}ZnDMb/ZnDMb isosbestic points. The kinetic time-courses for the ET intermediates obtained with the reverse titration protocol indicate the occurrence of intracomplex rather than Stern−Volmer quenching and illustrate a new strategy for characterizing low-affinity, highly reactive ET complexes. Our results for the [ZnDMb, Feb_5] complex further show that the ET cycle of eqs 2 and 3 cannot be described by a simple kinetic mechanism in which the complex adopts a single binding conformation. Measurements of the timecourse for the ET quenching reaction, eq 2, show that the **^{3}DA** complex and, by inference, the **DA** complex is kinetically labile, with a dissociation rate constant of k_{off}(**^{3}DA**) = k_{off}(**DA**) > 10^4 s^{-1} and a low association constant. However, the charge transfer intermediate, **I**, is less labile, providing evidence of ET-linked changes at the protein−protein interface. A minimum of three kinetic phases is needed to describe the full set of progress curves of **I**, at least two of which are *intra*complex. This implies that the [ZnD^+Mb, $Fe^{2+}b_5$] complex exhibits at least two kinetically distinct conformations with different ET rates for return to the **DA** ground state and that they interconvert at rates that compete with ET. It further appears that the conformer produced by photoinitiated ET is the most reactive and that it converts to one or more forms with progressively lower ET reactivities and decreased upper bounds on the rates of dissociation.

As a first step toward understanding the structural basis of interfacial recognition between Mb and b_5 we have used Brownian dynamics simulations[20] to generate encounter complex(es) at several pH values. These calculations show that Mb has a broad reactive surface which encompasses the "hemisphere" that includes the exposed heme edge. The most stable complexes occur when b_5 is bound at one of two subdomains within this hemisphere. The kinetics measurements and calculations taken together allow us to discuss the relative importance of global and local electrostatics in regulating protein−protein recognition and reactivity.

Experimental Procedures

Protein Preparation. Recombinant bovine tryptic cytochrome b_5 (b_5) was expressed in and isolated from *E. coli*. The gene coding for the tryptic form of the protein had been constructed by deletion of N- and C-terminal sequences from the lipase form and expressed in the same system used to express the lipase-solubilized protein.[21] The trypsin-solubilized recombinant protein has a sequence[21] identical to that of the trypsin-solubilized b_5 isolated from bovine liver.[22,23] The kinetics obtained with the recombinant protein were identical to those obtained with the hepatic protein.

Zinc-protomyoglobin (ZnPMb) was prepared from sperm whale myoglobin (Sigma Chemical Co., Type II) as described previously.[24] A similar procedure was used to prepare zinc-deuteromyoglobin (ZnDMb). Apomyoglobin (apoMb), prepared using the method of Teale,[25] was dialyzed at 4 °C against 4 L of 0.6 mM $NaHCO_3$ containing 1 mM Na_2EDTA and then twice against 4 L of 0.6 mM $NaHCO_3$. The final concentration of apoMb was ∼0.4 mM (ϵ_{280} = 15.4 mM^{-1} cm^{-1}).[26,27] ZnDP (Porphyrin Products, Logan, UT) was dissolved in a minimal volume of 0.1 M NaOH in the absence of light, centrifuged to remove any insoluble material, and diluted with water to give a 10 mM NaOH solution. All subsequent procedures were carried out in the absence of light at 4 °C. A 1.5-fold molar excess of the porphyrin stock solution was added dropwise with gentle stirring to apoMb at ∼4 °C. Reconstitution was usually complete within 1 h as monitored by a red shift of the Soret band. The protein solution was adjusted from pH ∼ 8 to pH 7.5 with 0.1 M HCl and concentrated by ultrafiltration (Amicon Centriprep-10) to a volume of 10 mL. To remove excess ZnDP, the protein solution was loaded onto a 1.5-cm × 30-cm gel filtration column (Sephadex G-25, Sigma) equilibrated with 25 mM potassium phosphate (KPi) buffer (pH 6.0), and ZnDMb was eluted with the equilibrating buffer.

ZnDMb was further purified by HPLC (Waters 650). The reconstitution mixture (∼100 mg in 20 mL) was loaded onto a TSK-based cation-exchange column (Beckman, 21.5 mm x 15 cm, SP-5PW) that had been pre-equilibrated with 25 mM KPi buffer at pH 6 (buffer A). Several minor components accounting for 25−50% of the total sample mixture eluted within a 90-min linear gradient in which the mobile phase (a mixture of buffer A and 25 mM K_2HPO_4) was pumped through the column at 5 mL/min. The major protein component was subsequently eluted by further increasing the pH with 25 mM K_3PO_4. The absorbance was monitored at 280, 414, and 575 nm (Waters 490 D multichannel detector). Both the minor component that elutes near 54 min and the major band (Figure 1) were collected. Despite the large difference in pI between these two components, we find that they have identical lifetimes and react similarly with b_5. The protein fractions were concentrated by ultrafiltration, and purified ZnDMb ($R_z = A_{414}/A_{280} \geq 15$) was stored in liquid nitrogen.

Protein stock solutions for kinetic measurements were exchanged into working buffer prior to the experiment using Centricon-10 microconcentrators (Amicon). Samples for kinetic measurements were prepared in the dark under a nitrogen atmosphere and contained 2 mL of nitrogen-purged 10 mM KPi buffer, 10 mM D-glucose, 115 μg/mL glucose oxidase (Sigma, type X-S from *Aspergillus niger*), and 30 μg/mL thymol-free catalase from bovine liver (Sigma) to assure anaerobicity.[28] Typical Mb concentrations for normal titrations were in the range of 1−5 μM (ϵ_{414} = 364.1 mM^{-1} cm^{-1}).[29] For the normal titration experiments, aliquots of a 0.2−1.0 mM stock solution of $Fe^{3+}b_5$ (ϵ_{413} = 117 mM^{-1} cm^{-1})[30] were added to the ZnDMb solution with a gastight syringe under a nitrogen blanket using Schlenk techniques. For reverse titrations, aliquots of a 0.2−1.0 mM ZnDMb stock solution were added to a solution containing 20−30 μM $Fe^{3+}b_5$. Protein stock solutions were deaerated by gentle purging with N_2. Optical spectra were obtained with a Hewlett-Packard 8451A diode array spectrophotometer.

(18) Magner, E.; McLendon, G. *J. Phys. Chem.* **1989**, *93*, 7130−7134.
(19) Natan, M. J.; Kuila, D.; Baxter, W. W.; King, B. C.; Hawkridge, F. M.; Hoffman, B. M. *J. Am. Chem. Soc.* **1990**, *112*, 4081−4082.
(20) Northrup, S. H.; Thomasson, K. A.; Miller, C. M.; Barker, P. D.; Eltis, L. D.; Guillemette, J. G.; Inglis, S. C.; Mauk, A. G. *Biochemistry* **1993**, *32*, 6613−6623.
(21) Funk, W. D.; Lo, T. P.; Mauk, M. R.; Brayer, G. D.; MacGillivray, R. T. A.; Mauk, A. G. *Biochemistry* **1990**, *29*, 5500−5508.
(22) Cristiano, R. J.; Steggles, A. W. *Nucl. Acids Res.* **1989**, *17*, 799.
(23) Reid, L. S.; Mauk, A. G. *J. Am. Chem. Soc.* **1982**, *104*, 841−845.
(24) Zemel, H.; Hoffman, B. M. *J. Am. Chem. Soc.* **1981**, *103*, 1192−1201.
(25) Teale, F. W. J. *Biochim. Biophys. Acta* **1959**, *35*, 543.
(26) Stryer, L. *J. Mol. Biol.* **1965**, *13*, 482−495.
(27) LaMar, G. N.; Toi, H.; Krishnamoorthi, R. *J. Am. Chem. Soc.* **1984**, *106*, 6395−6400.
(28) Stankovich, M. T.; Schopfer, L. M.; Massey, V. *J. Biol. Chem.* **1978**, *253*, 4971−4979.
(29) Luchi, J.; Hoffman, B. M. Unpublished results from ICP experiments.
(30) Ozols, J.; Strittmatter, P. *J. Biol. Chem.* **1964**, *239*, 1018−1023.

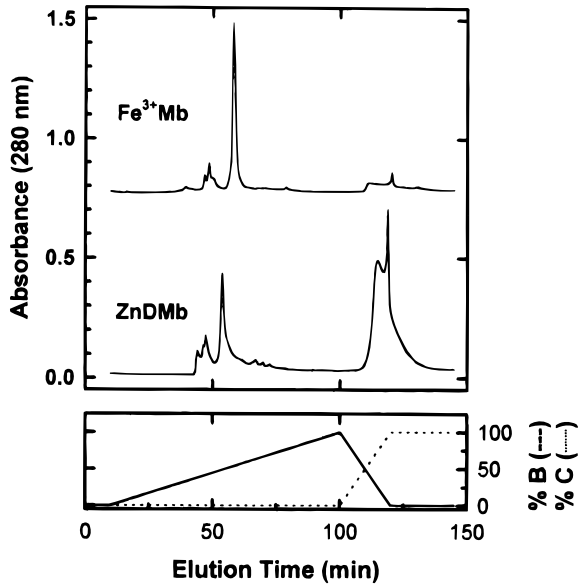

Figure 1. HPLC chromatograms for ZnDMb and Fe^{3+}Mb. Samples were loaded on a Beckman SP-5PW (2.15 cm × 15.0 cm) cation-exchange column equilibrated with 25 mM KPi buffer (pH 6). Proteins were eluted with a two-step procedure. In the first step, a 90-min linear pH gradient (right-hand axis) was generated by mixing 25 mM K_2HPO_4 (buffer B) with the starting buffer at a flow rate of 5 mL/min. In the second step, 25 mM K_3PO_4 was pumped through the column.

Data Collection and Processing. Photoexcitation was achieved with a Nd:YAG pulsed laser (Continuum, YG660A, 7 nsec pulse width, λ = 532 nm). The incident power was varied using a tunable polarizer (CVI Laser Corp.) and measured using a Scientech Model 372 power meter. For most experiments, the power was adjusted to achieve over 80% photolysis. The apparatus initially used for transient absorption[31] has a transient digitizer that collects data records of 2000 data points. As the progress curves for **I** encompass nearly three orders of magnitude in time, we collected data in paired segments on short and long timescale. These were merged into a single file so that the full progress curve could be fit. More recent data were acquired with a LeCroy Model 9310 digitizer. Because the LeCroy digitizer can accumulate 50 000 data points, the entire timecourse was collected in a single segment. To maintain maximal resolution at early times without losing resolution at long times, data were logarithmically compressed to a data record of 500 pretrigger points and ~3000 data points. For each laser flash, we acquired both a baseline signal and the transient signal. By subtracting the baseline signal from the data signal we can reliably measure $\Delta A = \pm 2 \times 10^{-4}$ OD even at long-times ($t \rightarrow 1$ s) where the transient signal is generally quite small ($\Delta A \leq 10^{-3}$ OD).

In the initial phase of this work, kinetic parameters were estimated by comparing experimental timecourses to those simulated with the GEAR software package.[32,33] This program does not iteratively fit data, and thus parameters were adjusted manually and simulations were repeated until the resultant simulated timecourse gave a satisfactory reproduction of the experimental data. Subsequently, we used version 3.4 of the SCoP program[34] which can both simulate and iteratively fit data curves, to numerically integrate the kinetic differential equations for the mechanisms under investigation.

Brownian Dynamics Simulations. Brownian dynamics simulations of the encounter complex(es) formed by b_5 and Mb were performed with the program BDTIRM as described by Northrup et al.[20] with an SGI Indy 2 R5000SC workstation. The reaction conditions assumed in these simulations were pH 6.0 and 7.5, 298.15 K, and μ = 20 mM. In these simulations, the models representing the two proteins were those derived from X-ray crystallographic analyses. Specifically, the coordinates of trypsin-solubilized $Fe^{3+}b_5$ were generated from those of lipase-solubilized bovine liver b_5[35] by deleting the coordinates for the N- and C-terminal residues absent from the trypsin-solubilized protein. The coordinates of sperm whale Fe^{2+}Mb[36] were used to represent the structure of Zn-substituted Mb. Both sets of coordinates were obtained from the Brookhaven Protein Databank.[37] The protonation state of each titratable group was assigned through use of the Tanford-Kirkwood procedure as modified by Matthew and co-workers.[38]

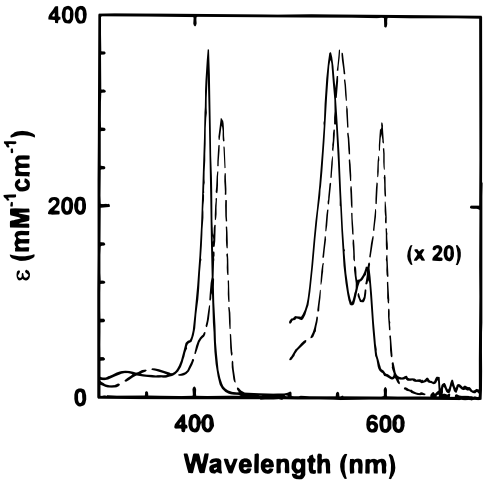

Figure 2. Electronic absorption spectra of ZnPMb (- -) and ZnDMb (—). *Conditions:* 10 mM KPi buffer, pH 7, ambient temperature.

Results

Spectral Properties. As electron transfer between ZnMb and Feb_5 is studied here by monitoring the color changes associated with the ET cycle of eqs 2 and 3, we begin by describing the optical spectra of ZnMb and b_5 in their various redox states. The absorption spectra of ZnPMb and ZnDMb are shown in Figure 2. The spectrum of ZnDMb is blue-shifted relative to that of ZnPMb, with maxima at 428, 554, and 596 nm for ZnPMb and 414, 542, and 580 nm for ZnDMb. Neither protein shows a spectral shift with pH, indicating that the zinc ion remains five-coordinate within the pH range studied in this paper, with the fifth ligand being His 93. The absorption spectra of b_5, as reported earlier,[30] have maxima at 412 and 532 nm for the oxidized state and 424, 528, and 556 nm for the reduced state, and both spectra are pH-independent.

Flash excitation of ZnMb (**D**) produces ^{1}ZnMb. The lifetime of the singlet state is a few nanoseconds,[39] and intersystem crossing to produce ^{3}ZnMb (^{3}**D**) is highly efficient ($\Phi \geq 0.80$). As our apparatus can only detect processes having rate constants $\leq 10^5$ s^{-1}, only the triplet state contributes to our measurements. Figure 3 shows the {^{3}**D** − **D**} difference spectra for ZnPMb and ZnDMb measured as the zero-time absorbance difference following flash photolysis. Among the salient features of the ZnPMb spectrum are the characteristic bleaching of the Soret absorbance (λ^-_{max} = 428 nm) and the positive absorbance changes between 437 and 547 nm (λ^+_{max} ~ 466 nm). The

(31) Wallin, S. A.; Stemp, E. D. A.; Everest, A. M.; Nocek, J. M.; Netzel, T. L.; Hoffman, B. M. *J. Am. Chem. Soc.* **1991**, *113*, 1842−1844.
(32) The GEAR program is available from Project Seraphim, Department of Chemistry, University of Wisconsin (Madison), 1101 University Avenue, Madison, WI 53706.
(33) Stabler, R. N.; Chesick, J. P. *Int. J. Chem. Kinetics* **1978**, *10*, 461−469.
(34) SCoP is available from Simulation Resources, Inc. in Berrien Spring, MI.
(35) Durley, R. C. E.; Mathews, F. S. *Acta Crystallogr.* **1996**, *D52*, 65−76.
(36) Phillips, S. E. V.; Schoenborn, B. P. *Nature* **1981**, *292*, 81−82.
(37) Bernstein, F. C.; Koetzle, T. F.; Williams, G. J. B.; Meyer, E. F. J.; Brice, M. D.; Rodgers, J. R.; Kennard, O.; Shimanouchi, T.; Tasumi, M. *J. Mol. Biol.* **1977**, *112*, 535−542.
(38) Matthew, J. B.; Gurd, F. R. N.; Garcia-Moreno, B. E.; Flanagan, M. A.; March, K. L.; Shire, S. J. *Crit. Rev. Biochemistry* **1985**, *18*, 91−197.
(39) Leonard, J. J.; Yonetani, T.; Callis, J. B. *Biochemistry* **1974**, *13*, 1460−1464.

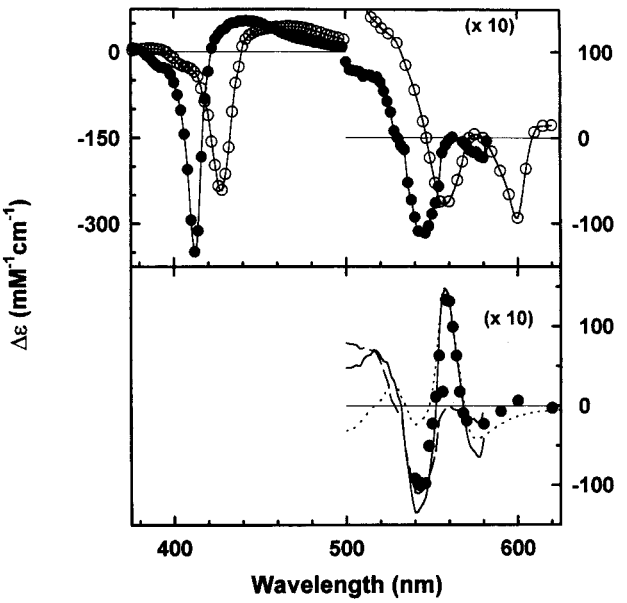

Figure 3. Difference spectra for Zn-substituted myoglobins and cytochrome b_5. Upper panel: {^{3}**D** − **D**} kinetic difference spectra for ZnPMb (○) and ZnDMb (●). Lower panel: Simulated static difference spectrum of the ET intermediate **I** (—), generated by combining the [$Fe^{2+}b_5$ − $Fe^{3+}b_5$] difference spectrum (···) and the [ZnD^+Mb − ZnDMb] difference spectrum (— —). The latter was approximated by shifting the ^{3}**D** − **D** spectrum (● in the upper panel) by 2 nm. The kinetic difference spectrum of **I** (●) was obtained from the time-resolved transient absorbance signal at $\tau = 65$ ms. *Conditions:* 10 mM KPi, pH 7.0, 20 °C.

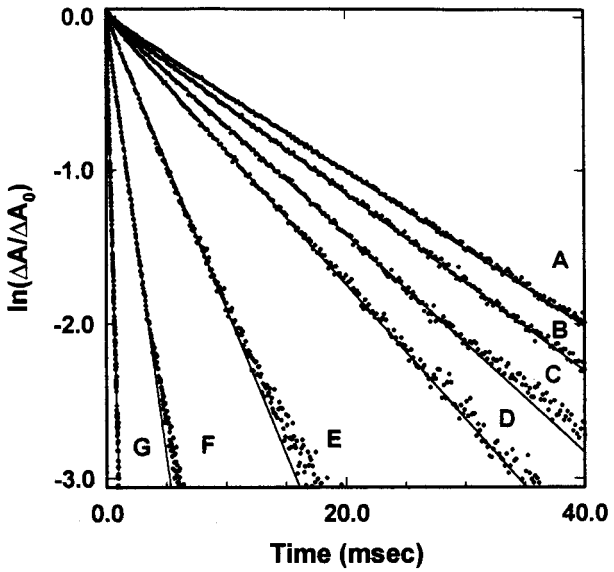

Figure 4. Triplet decay curves for the titration of ZnDMb with $Fe^{3+}b_5$ at pH 7.5 (A−D) and for the endpoint of titrations at pH 7.0 (E), pH 6.5 (F), and pH 6.0 (G). Traces were fit with an exponential decay function. (A−D), [ZnDMb] = 2.26 μM. (A) Without $Fe^{3+}b_5$ ($k_D = 50$ s^{-1}); (B) [$Fe^{3+}b_5$] = 3.02 μM ($k_{obs} = 58$ s^{-1}); (C) [$Fe^{3+}b_5$] = 8.91 μM ($k_{obs} = 70$ s^{-1}); (D) [$Fe^{3+}b_5$] = 14.6 μM ($k_{obs} = 86$ s^{-1}); (E) [ZnDMb] = 1.68 μM, [$Fe^{3+}b_5$] = 11.9 μM ($k_{obs} = 190$ s^{-1}); (F) [ZnDMb] = 2.23 μM, [$Fe^{3+}b_5$] = 20.9 μM ($k_{obs} = 571$ s^{-1}); and (G) [ZnDMb] = 2.59 μM, [$Fe^{3+}b_5$] = 17.3 μM ($k_{obs} = 2990$ s^{-1}). *Conditions:* 10 mM KPi buffer, 20 °C, 475 nm.

spectrum of ZnDMb is blue-shifted relative to that of ZnPMb, with $\lambda^+_{max} \sim 442$ nm and $\lambda^-_{max} = 412$ nm. The wavelength where the absorbance difference is maximal (412 nm) is not optimal for monitoring ^{3}**D** decay because of interference from the {**I** − ^{3}**DA**} absorbance difference (see below); instead we monitor the decay of ^{3}ZnDMb at 475 nm, where the **I** − **DA** absorbance difference is negligible relative to the ^{3}**D** − **D** and ^{3}**DA** − **DA** absorbance difference.

The [$(ZnMb)^+$, $Fe^{2+}b_5$] electron-transfer intermediate (**I**) that forms upon flash photolysis of the [ZnMb, $Fe^{3+}b_5$] complex can be studied by monitoring transient-absorption changes. The **I** − **DA** difference spectrum is the sum of the difference spectra for the reduction of $Fe^{2+}b_5$ and the accompanying oxidation of ZnDMb: {**I** − **DA**} = [ZnD^+Mb, $Fe^{2+}b_5$] − [ZnDMb, $Fe^{3+}b_5$] = [$Fe^{2+}b_5$ − $Fe^{3+}b_5$] + [ZnD^+Mb − ZnDMb]. The $Fe^{2+}b_5$ − $Fe^{3+}b_5$ absorbance difference spectrum is shown in Figure 3. The optimal wavelengths for obtaining the full kinetic profile associated with **I** are the ^{3}**D**/**D** isosbestic points. As the isosbestic points for the reduction of b_5 (438 and 544 nm) are within 2 nm of the isosbestic points for the {^{3}ZnPMb − ZnPMb} difference spectrum, it is difficult to monitor changes in the redox state of b_5 immediately after flash excitation of ZnPMb. However, the absorption spectrum of ZnDMb shifts relative to that of ZnPMb in both the ground state (**D**) and the triplet state (^{3}**D**). As a result, the ^{3}**D**/**D** isosbestic points for the ^{3}ZnDMb/ZnDMb transient-absorbance difference shift from 437 and 547 nm for ZnPMb, to 421 and 562 nm, which places the isosbestic points for ZnDMb near the wavelength maxima for the {$Fe^{2+}b_5$ − $Fe^{3+}b_5$} difference spectrum (424 and 556 nm). Unlike the π-cation radical forms of Zn-substituted cytochrome c peroxidase[40] and Zn-substituted horseradish peroxidase,[41] ZnD^+Mb ($\mathbf{D}^+$) is not stable long enough to acquire its static spectrum. Instead, we approximated the ZnD^+Mb − ZnDMb absorbance difference by blue-shifting the ^{3}ZnDMb − ZnDMb kinetic difference spectrum (Figure 3). This spectrum was combined with the [$Fe^{2+}b_5$ − $Fe^{3+}b_5$] difference spectrum to predict the static {**I** − **DA**} difference spectrum shown in Figure 3. This predicted spectrum is dominated by the [$Fe^{2+}b_5$ − $Fe^{3+}b_5$] difference in the absorbance range 540−580 nm, and by the [ZnD^+Mb − ZnDMb] difference in the 600−700 nm range.

Triplet Quenching and Binding Estimates. In the absence of b_5, ^{3}ZnDMb decays to its ground state (Figure 4) with a rate constant, $k_D = 52 \pm 5$ s^{-1}, that is slightly less than that for ^{3}ZnPMb ($k_D = 70$ s^{-1}).[24] The decay profile is exponential for at least 3 half-lives, and k_D is independent of pH. Addition of $Fe^{2+}b_5$ does not quench ^{3}ZnDMb (data not shown), whereas addition of $Fe^{3+}b_5$ gives quenching. Figure 4 shows the triplet decay curves acquired at 475 nm at several stages during a titration of ZnDMb with $Fe^{3+}b_5$ at pH 7.5 (10 mM KPi buffer) and those for the final points of titrations at pH 6.0, 6.5, and 7.0. The decay profiles remain exponential throughout all the titrations. At pH 7.5, the observed decay rate constant (k_{obs}) increases minimally, from $k_D = 52$ s^{-1} (in the absence of b_5) to $k_{obs} = 80$ s^{-1} at the final point, where [$Fe^{3+}b_5$]/[ZnDMb] = 6.5. The quenching increases dramatically as the pH is lowered, with $k_{obs} = 190$, 571, and 2990 s^{-1} at the final points of the titrations at pH values of 7.0, 6.5, and 6.0. Figure 5 is a plot of $\Delta k = k_{obs} - k_D$ obtained during the normal titrations of ZnDMb with $Fe^{3+}b_5$ in 10 mM KPi buffer at pH values of 6.0, 6.25, 6.5, 7.0, and 7.5. At all pH values, Δk increases linearly upon addition of $Fe^{3+}b_5$.

We have also measured the triplet quenching rate constant during a reverse titration in which aliquots of ZnDMb were added to a solution containing a fixed concentration of $Fe^{3+}b_5$ such that the concentration of $Fe^{3+}b_5$ was always in excess relative to the concentration of ZnDMb. Throughout this

(40) Liang, N. Ph.D. Dissertation, Northwestern University, Evanston, IL, **1988**.

(41) Kaneko, Y.; Tamura, M.; Yamazaki, I. *Biochemistry* **1980**, *19*, 5795−5799.

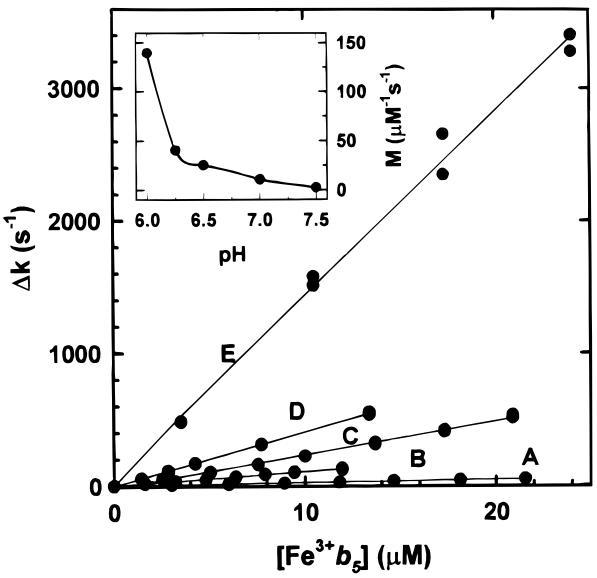

Figure 5. Triplet quenching of ZnDMb as a function of $[Fe^{3+}b_5]_{total}$ at pH 6.0 (E), pH 6.25 (D), pH 6.5 (C), pH 7.0 (B), and pH 7.5 (A). The solid lines are fits to eq 6 as described in the text using the parameters given in Table 1. Inset: pH dependence of the slopes (M) obtained from these titration curves. *Conditions:* [ZnDMb] ~ 1−3 μM, 10 mM KPi buffer, 20 °C.

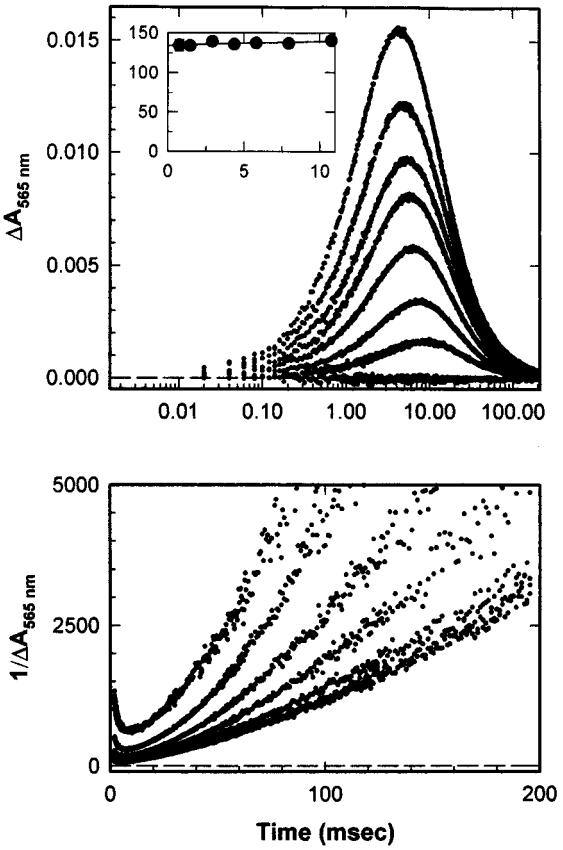

Figure 6. Progress curves for the ET intermediate generated during the reverse titration of $Fe^{3+}b_5$ with aliquots of ZnDMb. Inset: Triplet quenching as a function of [ZnDMb]. *Conditions*: 10 mM KPi buffer, pH 7, 20 °C; $[Fe^{3+}b_5]$ = 24.5 μM; [ZnDMb] = 0, 0.74, 1.5, 3.0, 4.4, 5.9, 8.0, and 10.8 μM, from bottom to top (upper) or top to bottom (lower).

experiment, the triplet decay traces were exponential for at least three half-lives. The inset to Figure 6 shows the triplet quenching rate constant (Δk) obtained for the reverse titration

Scheme 1

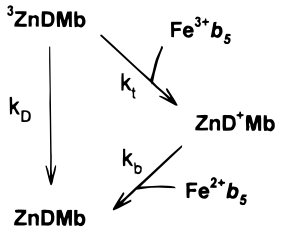

Scheme 2

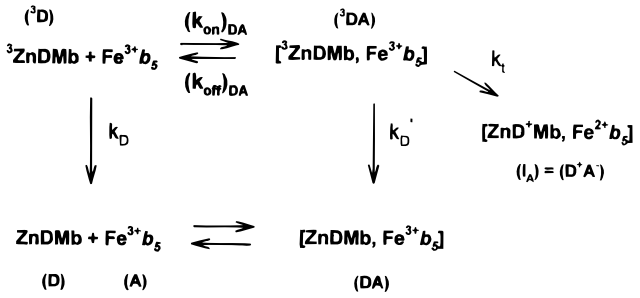

at pH 7. In this experiment, Δk was nearly constant for 1 μM < [ZnDMb] < 10 μM.

The linearity of the normal titrations (Figure 5) and the nearly zero slope of the inverse titration (Figure 6, inset) are consistent with the simple collisional, Stern−Volmer quenching mechanism illustrated in Scheme 1, which does not require the existence of a [^{3}ZnDMb, $Fe^{3+}b_5$] complex. However, the linear titration plots also are consistent with a kinetic model (Scheme 2) involving a dynamic equilibrium between the [^{3}ZnDMb, $Fe^{3+}b_5$] complex (**^{3}DA**) and its unbound components (**^{3}D** and **A**) in the limit where $[\mathbf{A}]/K_D = K_A[\mathbf{A}] \ll 1$, where K_D and K_A are the dissociation and association constants. Although the triplet quenching data does not require the inclusion of a bound complex, we explore the dynamic equilibrium mechanism to determine limiting values for the association constant and because consideration of the kinetic behavior of the intermediate formed by quenching (see below) requires the existence of a pre-formed **^{3}DA** complex.

Scheme 2 leads to exponential triplet decays when the exchange between the complex and its components is fast ($k_{off} \gg k_D + k_t$). In this case, the observed decay constant is the weighted average of the rate constants for **^{3}D** and **^{3}DA** decay

$$k_{obs} = k_D + \Delta k$$
$$= k_D + k_q f \quad (4)$$

Here, $\Delta k \equiv k_q f$ is the observed quenching rate constant, k_q is the intracomplex quenching rate constant, and f, the fraction of ^{3}ZnDMb that resides in the **^{3}DA** complex at equilibrium, is described by eq 5

$$f = \frac{K_D + \boldsymbol{D} + \boldsymbol{A} - \sqrt{(K_D + \boldsymbol{D} + \boldsymbol{A})^2 - 4\,(\boldsymbol{D})\,(\boldsymbol{A})}}{2\,\boldsymbol{D}} \quad (5)$$

where **D** is the total concentration of ZnDMb, **A** is the total concentration of $Fe^{3+}b_5$ added, and K_D is the dissociation constant. In the limit where $[\mathbf{A}]/K_D = K_A[\mathbf{A}] << 1$, eqs 4 and 5 reduce to

$$\Delta k = k_q K_A [Fe^{3+}b_5] = M[Fe^{3+}b_5] \quad (6)$$

The solid lines in Figure 5 are fits to eq 6 for the experimental data. The slope ($M = K_A k_q$) obtained from such plots of Δk versus $[Fe^{3+}b_5]_{total}$ (Table 1 and Figure 5, inset) increases sharply with decreasing pH, going from 2.4 × 10^6 M^{-1} s^{-1} at pH 7.5

Table 1. Parameters Describing the Formation of the [^{3}ZnDMb, $Fe^{3+}b_5$] Complex[a]

pH	M^b (μM^{-1} s^{-1})	$(k_q)_{min}{}^c$ (s^{-1})	$(k_{off})_{min}{}^d$ (s^{-1})
6.0	140	4.6×10^4	1×10^6
6.25	41	1.4×10^4	2×10^5
6.5	25	8.2×10^3	1×10^5
7.0	11	3.6×10^3	5×10^4
7.5	2.4	7.9×10^2	1×10^4

[a] 10 mM KPi, 20 °C. Values of M have uncertainty of ±10%. [b] $M = k_qK_A$ (eq 6). [c] Obtained from M using $(K_A)_{max} = 3000$ M^{-1} in eq 6 (see text). [d] Determined by simulating the kinetic progress curves as discussed in text.

to 140×10^6 M^{-1} s^{-1} at pH 6.0. The increase in the slope with lowered pH reflects an increase in the affinity constant, the quenching rate constant, or some combination of these. To establish an upper limit for K_A and a corresponding lower limit for k_q, we input a range of values for K_A into eqs 4 and 5 to generate a series of titration curves. The maximum allowable binding constant for a titration, $(K_A)_{max}$, and the corresponding minimum quenching constant, $(k_q)_{min}$, are those where the simulation does not exhibit noticeably more curvature than the experimental titration curve. As the experimental titrations at each pH involve roughly the same concentration of **D** ≈ 2 μM and the same range of concentrations for **A**, the absence of significant curvature at any pH leads to the limit $(K_A)_{max}$= 3000 M^{-1}. The $(k_q)_{min}$ calculated using $(K_A)_{max}$ = 3000 M^{-1} and the measured values of M increases roughly 60-fold with decreasing pH, going from 790 s^{-1} at pH 7.5 to 4.6×10^4 s^{-1} at pH 6.

From the $(K_A)_{max}$ and $(k_q)_{min}$ given in Table 1, it is possible to use the observation of exponential decay curves for the total triplet population ([^{3}**D**] + [^{3}**DA**]) to obtain a more precise lower limit of the dissociation rate constant for ^{3}**DA**, $(k_{off})_{min}$, than the intuitive one, $k_{off} \gg k_{obs}$. For each pH, we used Scheme 2 to simulate the triplet decay traces as a function of k_{off}; the minimum value of k_{off} for which the simulated decay traces remain exponential, $(k_{off})_{min}$, are given in Table 1. The minimum dissociation rate constants estimated in this fashion increase from $(k_{off})_{min} \sim 10^4$ s^{-1} at pH 7.5 to ~10^6 s^{-1} at pH 6.

For a reverse titration, the slope of a titration plot is a measure of the association constant, while the intercept (k_0) is dependent on M, K_A, and $[\mathbf{A}]_0$. When both the slope and the intercept can be measured, it is possible to determine both K_A and the intracomplex ET rate constant (k_q). Although the reverse titration gives a precise value for the intercept (k_0 = 135 s^{-1}), the slope for the reverse experiment shown in Figure 6 is too small to be reliably measured.

We further considered whether more reliable estimates of K_A and k_q can be obtained by combining the parameters from the two titration experiments. The association constant can be obtained with eq 7

$$K = \frac{M}{k_0} - \frac{1}{[\mathbf{A}]} \qquad (7)$$

where [**A**] is the concentration of the quencher ($Fe^{3+}b_5$) in the reverse titration, k_0 is the intercept obtained from a reverse titration, and M is the slope obtained from a normal titration. Using M = 8.8 (2) μM^{-1} s^{-1} and k_0 = 135 (10) s^{-1} for [**A**] = 24.5 μM in eq 7 gives K_A ranging from 6100 M^{-1} to 4.6×10^4 M^{-1}, which is quite consistent with the $(K_A)_{max}$ = 3000 M^{-1} we estimated from the normal titration.

Charge-Separated Intermediate. The kinetic behavior of the intermediate (**I**) formed through quenching of ^{3}ZnDMb by $Fe^{3+}b_5$ was examined during the course of normal and reverse titrations. Figure 6 shows the transient-absorbance changes for **I** at the 562 nm ^{3}**D/D** isosbestic point obtained during the pH 7 reverse titration of $Fe^{3+}b_5$ with ZnDMb, and Figure 7 shows the transient signals for the normal titration of ZnDMb with $Fe^{3+}b_5$, at pH 7.5.

These signals persist after ^{3}ZnDMb has disappeared, and thus the full time-resolved absorbance-difference spectrum for **I** could be collected at long-times. A representative plot of $\Delta A(\tau = 65$ ms) versus wavelength is shown in Figure 3 for 520 nm < λ < 620 nm. The kinetic difference spectrum obtained in this way agrees well with the simulated {**I** − **DA**} difference spectrum, which is predominantly associated with the reduction of $Fe^{3+}b_5$. In addition, the transient difference spectrum measured at 50 ms shows a maximum near 670 nm, as expected for ZnD^+Mb, and it has the same kinetic behavior as seen at wavelengths dominated by $Fe^{3+}b_5$ reduction. Thus, the redox-related absorbance changes associated with ZnD^+Mb and $Fe^{2+}b_5$ are kinetically correlated.[42]

Although it is not possible to examine the full wavelength dependence of this transient for $\tau \leq 5/k_{obs}$ without interference from the {^{3}**D** − **D**} absorbance difference, the full timecourse of the transient is observable at ^{3}**D/D** isosbestic points (Figures 6 and 7). The absorbance changes at both the 421 and 562 nm ^{3}**D**/**D** isosbestic points are positive, with the magnitude at the former being nearly six times greater than the latter (data not shown). Both observations are consistent with the expected difference spectrum of the ET intermediate (Figure 3). Thus, the quenching of ^{3}ZnDMb by $Fe^{3+}b_5$ is indeed associated with the ^{3}ZnDMb → $Fe^{3+}b_5$ ET process (eq 2) and the return to the ground state with eq 3.

Kinetic Model (Scheme 3) for I. The triplet quenching data is consistent with either the collisional Stern−Volmer mechanism (Scheme 1) or with Scheme 2 in the rapid-exchange limit where K_A < 3000 M^{-1} and k_{off} > 10^4 s^{-1}. If triplet quenching occurs by this limit of Scheme 2 *and if the* $\boldsymbol{D^+A^-}$ *product is also weakly bound and kinetically labile*, then the products that persist after the complete decay of ^{3}ZnDMb are unbound ZnD^+Mb and $Fe^{2+}b_5$, and the decay of the ET transient signal must be second-order at long times. If, instead, triplet quenching occurs by a Stern−Volmer mechanism without formation of a precursor complex, then the *only* products are the unbound protein components (ZnD^+Mb and $Fe^{2+}b_5$), and again the long-time decay of the ET transient signal must necessarily be second-order.

To test these predictions, we examined the long-time behavior ($t \geq 5/k_{obs}$) of the progress curves of the ET intermediate during the course of a normal titration and a reverse titration. Figures 6 and 7 show the transient absorbance signals for **I** obtained during the pH 7 reverse titration and the pH 7.5 normal titration, respectively. In the normal titration, the amplitude of the transient signal increases monotonically upon addition of $Fe^{3+}b_5$,

(42) Alternative mechanisms involving a third redox center (R) on either ZnDMb (eq 8) or Feb_5 (eq 9)

$$[(ZnD^+R)Mb, (Fe^{2+})b_5] \rightleftarrows [(ZnDR^+)Mb, (Fe^{2+})b_5] \qquad (8)$$

$$[(ZnD^+)Mb, (Fe^{2+}R)b_5] \rightleftarrows [(ZnD)Mb, (Fe^{2+}R^+)b_5] \qquad (9)$$

with appropriate dissociation steps for either would require that one or more of the kinetic phases is spectroscopically different from the others, and thus there would be differences in the kinetic behavior seen at wavelengths that are dominated by redox changes involving the heme of b_5 (540 nm to 580 nm) and those involving ZnDMb (λ > 600 nm). However, as we noted in the text, the absorbance changes at wavelengths associated with ZnDMb are kinetically correlated with those at wavelengths associated with b_5.

(43) Northrup, S. H.; Reynolds, J. C. L.; Miller, C. M.; Forrest, K. J.; Boles, J. O. *J. Am. Chem. Soc.* **1986**, *108*, 8162−8170.

(44) Stemp, E. D. A.; Hoffman, B. M. *Biochemistry* **1993**, *32*, 10848−10865.

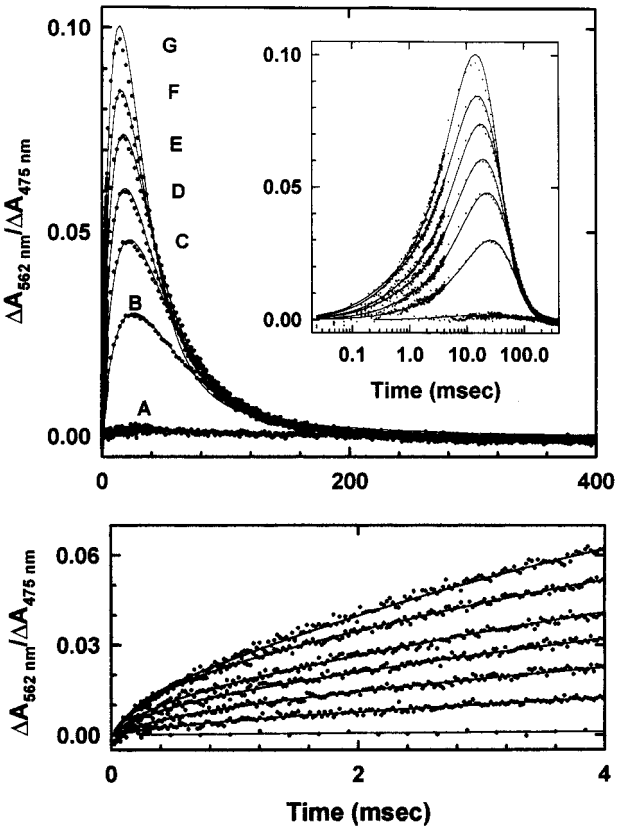

Figure 7. Absorbance transients generated by photoinitiated ET during the normal titration of ZnDMb (pH 7.5) with $Fe^{3+}b_5$ on short (Lower panel) and long (Upper panel) time scales. Inset: Transient signals plotted on a logarithmic time scale to emphasize the early-time data. To compensate for differences in the triplet yield during the titration, we have referenced the absorbance changes to the zero-time yield of triplet (ΔA_0 at 475 nm). See ref 44. *Conditions:* $[ZnDMb]_{total} = 2.26$ μM, 10 mM KPi buffer, pH 7.5, 20 °C. (A) in the absence of $Fe^{3+}b_5$; (B) $[Fe^{3+}b_5] = 5.99$ μM; (C) $[Fe^{3+}b_5] = 8.91$ μM); (D) $[Fe^{3+}b_5] = 11.8$ μM; (E) $[Fe^{3+}b_5] = 14.6$ μM; (F) $[Fe^{3+}b_5] = 18.1$ μM and (G) $[Fe^{3+}b_5] = 21.5$ μM.

as does the quenching rate constant. Because Δk changes during a normal titration, the shape of the ET transient curve must also change during a titration. Thus, shape changes arising from concentration-dependent, second-order contributions to the thermal back ET reaction are not easily detected without a full mechanistic analysis of the progress curves. In contrast, Δk is essentially invariant during a reverse titration (Figure 6, inset), and, thus, any systematic shape changes can only be associated with the thermal back ET reaction. We therefore focus our attention on the analysis of the reverse titration.

If the timecourse of the $\mathbf{A}^- \rightarrow \mathbf{D}^+$ back reaction were second-order for $t > 5/k_{obs}$, a plot of $1/\Delta A$ vs. time would be linear and the data taken during a reverse titration would give a set of lines having identical slopes. The experimental plots of $1/\Delta A$ vs. time obtained during the pH 7 reverse titration are shown in Figure 6. In fact, the experimental progress curves diverge at long times during the reverse titration. These observations are inconsistent with the prediction for a second-order reaction and require instead that part of the $Fe^{2+}b_5 \rightarrow ZnD^+Mb$ ET reaction occurs by a first-order process within the $\boldsymbol{D}^+\boldsymbol{A}^-$ product complex. Given that the product of the photoinitiated ET reaction is the $\boldsymbol{D}^+\boldsymbol{A}^-$ complex, it follows that this reaction occurs within a ^{3}**DA** precursor complex. Thus, triplet quenching does not occur by a collisional, Stern−Volmer mechanism but instead occurs by the rapid-exchange limit of Scheme 2.

Scheme 3

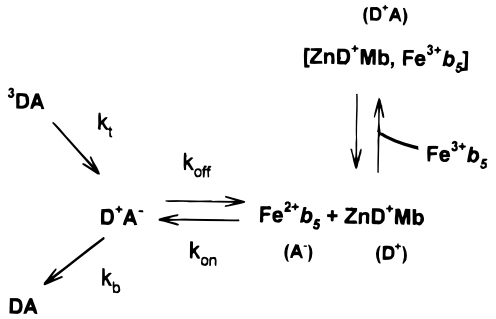

As a first step toward making this conclusion more quantitative, we consider a *minimal* mechanism that includes dynamic complex formation and intracomplex ET for both the forward and reverse reactions as embodied in the combination of Scheme 3 with Scheme 2. In this mechanism, the $\boldsymbol{D}^+\boldsymbol{A}^-$ complex produced by the photoinitiated ET reaction can return to the ground state by intracomplex $Fe^{2+}P \rightarrow ZnD^+$ ET (rate constant k_b) or it can dissociate (k_{off}) into its components, ZnD^+Mb and $Fe^{2+}b_5$, in a competing process. Subsequent second-order recombination of ZnD^+Mb and $Fe^{2+}b_5$ (k_{on}) completes the ET cycle. As the experiments are performed under conditions where the concentration of $Fe^{3+}b_5$ far exceeds the concentrations of all other species, in particular that of $Fe^{2+}b_5$, the mechanism further incorporates association of $Fe^{3+}b_5$ and ZnD^+Mb. In principle, this might be important because if ZnD^+Mb is sequestered in the electron-transfer inert $[ZnD^+Mb, Fe^{3+}b_5]$ complex ($\mathbf{D}^+\mathbf{A}$) it cannot react with $Fe^{2+}b_5$, and, therefore, the return of the electron transfer intermediate to the ground state complex is inhibited.

By appropriate selection of the kinetic parameters in Scheme 3, the behavior of the kinetic progress curves generated with this model can be made to vary from purely first-order, through mixed-order, to purely second-order. In the upper panel of Figure 8, we present three simulated progress curves that illustrate how the kinetic parameters can be varied so as to achieve this progression. The concentrations of reactants are those of one point in the middle of a reverse titration, that having $R \equiv [\mathbf{A}]/[\mathbf{D}] = 5$, and the simulations are "normalized" to $1/\Delta A \sim 2500$ at 150 ms, so that each progress curve for the ET transient persists over roughly the same time interval as the experimental data (Figure 6). The parameters that are critical for determining the kinetic behavior of the simulations are the association rate constant (k_{on}), the total decay rate constant for the $\boldsymbol{D}^+\boldsymbol{A}^-$ complex ($\Sigma = k_b + k_{off}$), and the fractional yield of dissociated ET products ($f_{off} = k_{off}/\Sigma$). The resulting parameter sets for each of the three regimes were then used to model the full reverse titration in which the donor concentration was varied 20-fold from $R = 25$ to $R = 1.25$.

The charge recombination reaction is calculated to be second-order in the rapid-exchange limit, where neither the ^{3}**DA** complex nor the $\boldsymbol{D}^+\boldsymbol{A}^-$ complex is present in detectable amounts because both complexes are weakly bound and kinetically labile. This limit is achieved only when $\Sigma > k_b > k_{obs}$ and k_{on} is large. Figure 8A uses one combination of parameters that satisfies the experimental normalization constraint of $1/\Delta A = 2500$ at 150 ms: $k_{on} = 4.5 \times 10^8$ M^{-1} s^{-1}, $\Sigma = 5 \times 10^5$ s^{-1}, and $f_{off} = 0.8$. The straight line calculated for the time dependence of $1/\Delta A$ is substantially different from the experimental results for the $R = 5/1$ point in the reverse titration (Figure 6).

The opposing, intracomplex limit, where the progress curves show first-order kinetic behavior at long times, occurs when ET within the kinetically labile ^{3}**DA** complex produces an

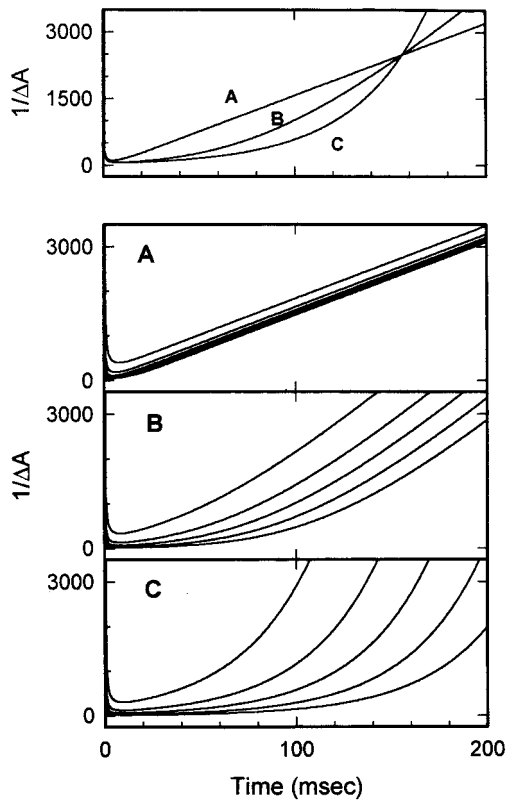

Figure 8. Simulated kinetic progress curves for the ET intermediate in the three limiting cases of Scheme 3. Upper panel: $R = [\mathbf{A}]/[\mathbf{D}] = 5$. The simulations have been normalized to $1/\Delta A \sim 2500$ at 150 ms, so that each transient persists over roughly the same time interval as the experimental data in Figure 6. Lower Panel: Simulated reverse titrations for the second-order limit (A), the mixed-order limit (B), and the intracomplex, first-order limit (C). *Conditions*: $[\mathbf{A}]_0 = 25\ \mu$M; $[\mathrm{D}]_0 = 1$, 2.5, 5.0, 10.0, and 20 μM (top to bottom). *Kinetic parameters*: See text.

intermediate that, in contrast, does not dissociate during the lifetime of the ET intermediate, **I**. This behavior is achieved with Scheme 3 by setting $k_{off} = 0$. The result is a simple kinetic cycle where **I** is formed according to Scheme 2 and returns to the **DA** state by intracomplex **I** → **DA** ET. In this case, the transient absorbance signals would rise with the larger of the $Fe^{2+}b_5 \rightarrow ZnD^{+}Mb$ thermal ET rate constant (k_b) and the triplet decay constant (k_{obs}) and subsequently disappear with the smaller of the two rate constants. To achieve the desired signal intensity at 150 ms, this limit requires $k_b \approx 20-30\ s^{-1} < k_{obs}$. The resulting plot of $1/\Delta A$ vs. time presented in Figure 8C is indeed curved, but far more so than is observed for the experimental data, suggesting that both intracomplex and second-order processes contribute to the observed ET transient signal. The intermediate, mixed-order regime of Scheme 3 involves both first-order kinetic contributions from the $\boldsymbol{D}^{+}\boldsymbol{A}^{-}$ complex as well as second-order contributions from its dissociated components, $\mathbf{D}^{+}$ and $\mathbf{A}^{-}$. To model the curvature in the plot of $1/\Delta A$ vs. time for the $R = 5$ point of the reverse titration, while maintaining the desired value of $1/\Delta A = 2500$ at 150 ms, requires that Σ be more than three orders of magnitude less than its value in the rapid-exchange limit ($\Sigma = 5 \times 10^5\ s^{-1}$); the mixed-order curve in Figure 8B uses $\Sigma = 100\ s^{-1}$. Because $k_{off} < \Sigma = k_b + k_{off} \sim 100\ s^{-1}$, this result then requires that k_{off} for the $\boldsymbol{D}^{+}\boldsymbol{A}^{-}$ complex be at least 100-fold less than $(k_{off})_{min} = 10^4\ s^{-1}$ as determined above (Table 1) for the precursor ^{3}**DA** complex.

Figure 8 also presents progress curves for the full reverse titrations as simulated with the kinetic parameters for each of the three regimes of Scheme 3. The result for $t \geq 5/k_{obs}$ is a suite of parallel lines, as expected for a second-order process, and this is at variance with the experimental reverse-titration traces (Figure 6) which diverge at long times. The progress curves calculated for the intracomplex limit (Figure 8C) are clearly nonlinear but with similar curvature throughout the titration and again differ from the experimental progress curves. When parameters are chosen so that the kinetics are mixed-order, and the progress curves include contributions from both recombinations of the dissociated components of **I** and from the undissociated $\boldsymbol{D}^{+}\boldsymbol{A}^{-}$ complex (Figure 8B), the resulting simulations reproduce the general trends in the experimental data; the simulations, like the experimental progress curves, diverge during the course of a reverse titration. Whereas the ^{3}**DA** complex is kinetically labile, dissociating in times of $t \ll 1/k_{obs}$, we conclude that at least some fraction of the charge-separated intermediate that is produced by ^{3}**D** → **A** ET is kinetically stable for times $t \gg 1/k_{obs}$.

Short-Time Behavior. The parameters required to model the long-time data for **I** require $\Sigma < k_{obs}$, in which case the scheme requires that the transient signal appear with a rate constant of k_{obs}. However, careful examination of the short-time behavior of **I** shows the rise rate is much greater than k_{obs}, with $k_{rise} \sim 10^3\ s^{-1}$, in which case even Scheme 3 cannot rigorously describe the data. A minimal mechanism required by this result must incorporate two conformers of **I**, one associated with the rapid rise ($\mathbf{I_A}$) and the second ($\mathbf{I_B}$) being the one whose long-time properties have been the focus of these investigations. The initial product of the photoinitiated ET would be $\mathbf{I_A}$, and the rise rate constant would be the return ET rate, plus the rate of the $\mathbf{I_A} \rightarrow \mathbf{I_B}$ conformational interconversion, plus the dissociation rate constant for $\mathbf{I_A}$, with $\Sigma = k_{rise} \approx 10^3\ s^{-1}$.

Brownian Dynamics Simulations. The encounter complexes formed by Fe^{2+}Mb and $Fe^{3+}b_5$ at pH 6.0 and 7.5 were simulated by calculation of 10 000 Brownian dynamics docking trajectories as described above. The results of the simulations at pH 6.0 are summarized in Figure 9 in which the successful trajectories are represented by the structure of Mb surrounded by points that represent the centers of mass of interacting molecules of b_5. Figure 9A presents a "side" view of the surface where the points are projected onto a slice through the plane of the heme; Figure 9B presents a "front" view of the encounter surface showing the surface of Mb where the edge of the heme is partially exposed to solvent. Examination of Figure 9 shows that the interaction surface encompasses the protein hemisphere that includes the surface of Mb where the heme edge becomes partially exposed to solvent, but that this surface is relatively large and diffuse as might be expected for a complex of relatively low stability. The finding that the surface of Mb recognized by b_5 is highly asymmetric and that there are relatively extensive regions that are visited rarely, if ever, by an approaching molecule of b_5 is particularly noteworthy insofar as the electrostatic potential surface of Mb exhibits no asymmetry in charge distribution. However, the positive end of the Mb dipole does project into roughly the center of this surface.

Examination of the location of the b_5 molecules in the ten complexes that exhibit the greatest electrostatic stabilization reveals that the relative stabilities of complexes occurring within this interaction surface appear to be distributed nonrandomly and in a manner that is somewhat dependent on pH. For example, at pH 6 (Figure 9), there appear to be two clusters of points that suggest the existence of two subdomains (Of the ten most stable encounter complexes, three occur in one of these domains and seven occur in the other.) within this interaction

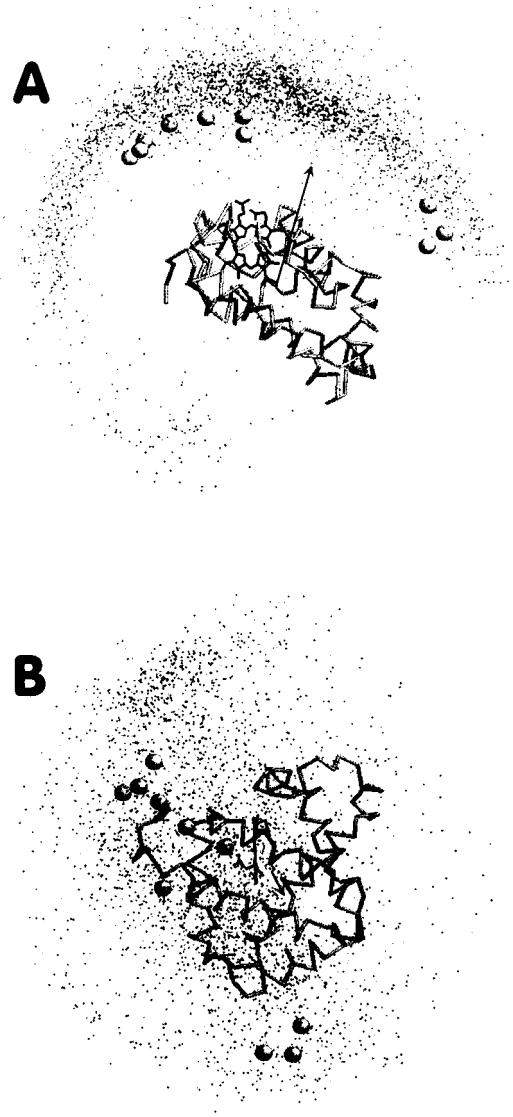

Figure 9. Docking profiles showing the target molecule, Mb, surrounded by dots that represent the centers of mass of $Fe^{3+}b_5$ for the encounter complexes formed with incoming $Fe^{3+}b_5$ molecules. For the ten complexes with the greatest electrostatic stabilization, the centers of mass of $Fe^{3+}b_5$ are presented as large spheres. *Conditions*: 298.15 K, μ = 20 mM; pH 6.0; (A) side view and (B) front view.

surface that provide greater electrostatic stabilization of the [Mb, b_5] complex. These two subdomains appear to persist at pH 7.5, but the distribution of b_5 molecules between the two (The ten most stable encounter complexes are divided equally between these two domains.) differs from that observed at lower pH (data not shown).

Figure 10 is a histogram that gives the frequency with which the individual charged surface residues of Mb and b_5 are involved in protein−protein contacts within the encounter complexes found by the Brownian dynamics simulations at pH 6.0. All of the electrostatic contacts involve acidic residues on the surface of b_5. In contrast, both acidic and basic charged residues of Mb are involved in contacts with high frequency. Thus, the low stability of the [Mb, b_5] complex compared to that of either the [cytochrome *c* peroxidase, cytochrome *c*] complex[43] or the [cytochrome b_5, cytochrome *c*][20] complex likely reflects the fact that in the former a large percentage of the local electrostatic interactions within the protein−protein interface are repulsive. Similar analysis of the trajectories resulting from the Brownian dynamics simulations performed at pH 7.5 identifies involvement of the same set of surface

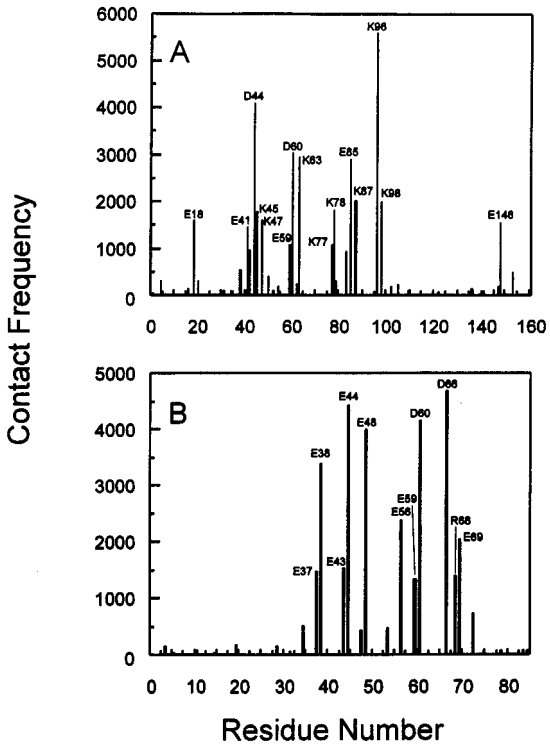

Figure 10. Histogram of frequencies at which individual charged residues of Fe^{2+}Mb (A) and $Fe^{3+}b_5$ (B) are involved in electrostatic interactions in 3360 encounter complexes predicted by Brownian dynamics simulations of 10 000 trajectories (μ = 20 mM, pH 6.0, and 298.15 K). Those residues involved in >1000 contacts are labeled.

residues of both proteins as being critical to complex formation, but the relative frequencies of contact differ somewhat (data not shown).

In a previous report, Livingston et al.[8] derived a model for the [Mb, b_5] complex through use of manual, graphical docking of the two proteins to optimize the number of interactions between charged surface residues. The structure predicted by Livingston et al. is contained within the surface binding region of Mb identified by the Brownian dynamics approach, but it does not lie within the densest region of the simulation. In fact, the majority of the complexes represented by the Brownian dynamics simulations do not resemble that of Livingston et al. with only ~100 of the ~3300 successful trajectories having their center of mass of b_5 within 25 Å of the three Mb surface Lys residues identified by Livingston et al.

The model described by Livingston et al. included interactions of Lys residues 47, 50, and 98 on the surface of Mb with the surface carboxylate residues Glu 43, Glu 44, Asp 60, and the heme 6-propionate group. With regard to the important surface residues of Mb, comparison of the results of the Brownian dynamics simulation with that model reveals that both methods identify Lys 47 and Lys 98 as important to protein−protein recognition, but the Brownian dynamics method does not implicate Lys 50. In addition, the Brownian dynamics method showed Lys residues 63 and 96 as having more frequent involvement in interaction with b_5, and Lys residues 45, 47, 77, 78, and 87 as having a somewhat lesser role. With regard to the surface residues of b_5, both approaches suggest significant roles for Glu 44 and Asp 60, though the Brownian dynamics approach places less emphasis on the role of Glu 43. Not surprisingly, the Brownian dynamics approach also identifies significant contributions by other charged surface residues of b_5, most notably Asp 66, Glu 38, and Glu 48.

Discussion

In this work, we have presented kinetic progress curves describing both the ^{3}ZnDMb → $Fe^{3+}b_5$, electron transfer process (eq 2) and the subsequent $Fe^{2+}b_5$ → ZnD^+Mb ET process (eq 3). The *minimal* kinetic description of the photoinitiated ET process must include formation of a weak but highly reactive precursor complex that is in dynamic equilibrium with its unbound components. Analysis of the quenching titration of ^{3}ZnDMb by $Fe^{3+}b_5$ indicated that the positively charged ZnDMb interacts only weakly with its negatively-charged partner $Fe^{3+}b_5$: for 6.0 < pH < 8.0, the maximum value for the association constant is $(K_A)_{max} \sim 3 \times 10^3$ M^{-1}, somewhat less than the value estimated from NMR experiments[8] with the [Fe^{3+}Mb(bovine heart), $Fe^{3+}b_5$(trypsin-solubilized, bovine liver)] complex ($K_A \sim 10^5$ M^{-1}, pH 5.6, 25 °C). The difference probably stems from the higher pH employed here, although it may, in part, reflect the fact that ZnDMb is an analogue of Fe^{2+}Mb, rather than Fe^{3+}Mb, and has a correspondingly lower net positive charge.

For each step in a titration of ZnDMb with $Fe^{3+}b_5$, the decay of ^{3}**DA** is exponential, which shows that the complex with $Fe^{3+}b_5$ is kinetically labile; $(k_{off})_{min}$ varies from 10^4 s^{-1} at pH 7.5 to 10^6 s^{-1} at pH 6. Consequently, the quenching data gives no information regarding the existence of multiple conformations of the ^{3}**DA** complex. If multiple conformations of ^{3}**DA** exist, they interconvert rapidly with respect to ^{3}ZnDMb → $Fe^{3+}b_5$ ET and the observed decay constants are weighted averages.

Transient absorption measurements have shown that this quenching of ^{3}ZnDMb by $Fe^{3+}b_5$ can be attributed to ^{3}ZnD → Fe^{3+}P ET, and that the transient absorbance changes observed at the ^{3}**D**/**D** isosbestic points represent the time evolution of the [ZnD^+Mb, $Fe^{2+}b_5$] intermediate, **I**. By modeling the experimental data, we have begun to identify the mechanistic requirements needed to completely describe the progress curves of the ET intermediate acquired during a reverse titration. First, the long-time behavior of the progress curves ($t \geq 20$ ms) shows neither pure second-order nor pure first-order kinetic behavior but rather resembles a mixed-order process involving both the undissociated ET product complex and its dissociated components. Modeling of the long-time behavior of **I** by Scheme 3 shows that some fraction of the $\boldsymbol{D}^+\boldsymbol{A}^-$ complex involved in this process must dissociate with a rate constant of $k_{off} < \Sigma = k_b + k_{off} \sim 100$ s^{-1}. Thus, this component appears to have a lifetime at least two orders of magnitude longer than that of the precursor, **DA**, complex! To what degree this sharp change in interfacial interactions reflects a thermodynamic property of the system and to what extent it represents a nonequilibrium, kinetically trapped state, remains to be explored.

These conclusions are supported by the model calculations based on Scheme 3 and presented in Figure 8. We have *not* attempted detailed fits to the data because careful examination of the early-time portion of the progress curve for the $\boldsymbol{D}^+\boldsymbol{A}^-$ intermediate suggests that there may be not one but two (or more) kinetically distinguishable conformers of the bound $\boldsymbol{D}^+\boldsymbol{A}^-$ complex. That formed directly by photoinitiated ET (denoted $\mathbf{I_A}$) decays through one of three channels: back ET, dissociation, or conformational interconversion to the conformer ($\mathbf{I_B}$) that governs the long-time behavior. The sum of these three rate constant for $\mathbf{I_A}$ corresponds to $k_{rise} \sim 10^3$ s^{-1} (as compared to a corresponding sum $\Sigma \sim 10^2$ s^{-1} for $\mathbf{I_B}$.) Thus, necessarily the rate constant for dissociation of $\mathbf{I_A}$ obeys the inequality $k_{off} < k_{rise}$, and so the lifetime of this conformer is at least 10-fold longer than that of the precursor **DA** complex. The existence of two subdomains within the interaction surface generated by Brownian dynamics is consistent with the kinetic experiments in that both approaches show that there are at least two conformers of the $\boldsymbol{D}^+\boldsymbol{A}^-$ complex. Extensive additional work will be required to fully characterize the rapidly reacting conformer and to achieve a complete kinetic description of this system.

Clearly, the apparent simplicities of the 1:1 binding and ET reaction between $Fe^{3+}b_5$ and ZnDMb masks a complicated coupling of interfacial recognition and electron-transfer. To this end, the diffuse nature of the Mb interaction surface generated by Brownian dynamics (Figure 9) emphasizes that there are a large variety of similarly stable structures for the [Mb, b_5] complex, a large number of which could be accessed during a reaction cycle. A static presentation of any one of these docked protein−protein complexes reveals only a limited set of interfacial contacts and masks the possible importance of other structures in the overall mechanism of ET. The Brownian dynamics simulations provide a more realistic view of the interaction surface.

The simulations emphasize the importance of global electrostatics in protein−protein recognition. Because there is no local patch of surface charge on Mb, one might expect that local electrostatic interactions would be relatively weak, and that the orientation of the dipoles might be the dominant steering force that aligns the molecular surfaces for ET. In support of this, we find that the dipole vector of Mb is directed toward the densest section of the interaction surface. The diffuse nature of the interaction surface and the low overall stability of the [Mb, b_5] complex(es) further suggests that a dominant set of local electrostatic interactions does not exist, but rather, there are a multitude of weak, local interactions that produce a variety of isoenergetic complexes. However, the kinetics suggests that not all conformations have comparable reactivities and that local interactions might play a key role in guiding the formation of the productive conformations.

Acknowledgment. This research has been supported by NIH Grant HL 13531 (B.M.H.), GM 33804 (A.G.M.), and NSF Grant MCB 9207974 (B.M.H.). We are grateful to Dr. Malin Kootsey for his assistance with the development of the SCoP models, to Dr. Scott Northrup for providing both the Brownian dynamics software and helpful discussions pertaining to its use, and to Dr. Joe Lakovits and Bob Loyd for their expert assistance with modifying the flash photolysis equipment.

JA9630811